Experiments and FEM Simulations of Fracture Behaviors for ADC12 Aluminum Alloy Under Impact Load

Yumei Hu[1,2*], Yue Xiao[1], Xiaoqing Jin[1], Haoran Zheng[1], Yinge Zhou[2], and Jinhua Shao[2]

[1]State Key Laboratory of Mechanical Transmission, Chongqing University,
Chongqing 400044, China
[2]State Key Laboratory of Vehicle NVH and Safety Technology, Chongqing 401122, China

Using the combination of experiment and simulation, the fracture behavior of the brittle metal named ADC12 aluminum alloy was studied. Five typical experiments were carried out on this material, with responding data collected on different stress states and dynamic strain rates. Fractographs revealed that the morphologies of fractured specimen under several rates showed different results, indicating that the fracture was predominantly a brittle one in nature. Simulations of the fracture processes of those specimens were conducted by Finite Element Method, whilst consistency was observed between simulations and experiments. In simulation, the Johnson-Cook model was chosen to describe the damage development and to predict the failure using parameters determined from those experimental data. Subsequently, an ADC12 engine mount bracket crashing simulation was conducted and the results indicated good agreement with the experiments. The accordance showed that our research can provide an accurate description for the deforming and fracture processes of the studied alloy.

1. INTRODUCTION

Lighter weight metals have received particular attention in the automotive industry, and many automobile components made by heavy steel have been replaced by cast aluminum alloys for their excellent physical properties such as ductility, strength, thermal and electrical conductivity and resistivity. However, brittle metallic components tend to rupture under impact loading. Therefore, it is necessary to study the fracture behaviors for brittle metal subjected to high speed impact load.

Studies on mechanical properties under impact loading have been focused on brittle nonmetals [1-5] and ductile metals [6-10]. For brittle nonmetallic materials, researchers have conducted studies on deforming and fracturing responses under dynamic loading by a combination of theoretical approach and laboratorial approach. Experiments [1-3] commonly include Split Hopkinson Pressure Bar and tensile tests. Based on the experimental results, constitutive models have been developed to describe the deformation and rupture process [4,5]. For instances, Johnson and Holmquist [4] proposed a modified Johnson-Cook model which was applicable for brittle materials subjected to large strain, high strain rate and high pressure. Jiang *et al.* [5] predicted the response of the axially loaded columns under impact loading by the concrete consti-

tution relationship embedded in LS-DYNA.

For ductile metals, the mechanical responses under impact loading have been studied by a variety of constitutive models, and these models include the Zerilli -Armstrong (Z-A)[11], the Cowper–Symonds (C-S) [12] and the Johnson–Cook (J-C) [13]. Among those models, the J-C model is perhaps the most widely used model [14]. To improve the accuracy of the J-C model, several modifications have been implemented including the strain softening, temperature softening and strain hardening terms of the J-C model [8,9].

For brittle metals, studies have been focused on the fracture mechanism [15-18]. However, few researches has been done about the deformation and rupture behaviors under impact loading, for the mechanical responses of brittle metals under high-speed impact are complicated and difficult to detect.

This paper aims to study the failure mechanisms and try to predict rupture behaviors of a typical brittle metal. We choose ADC12 aluminum alloy as a representation to describe the fracture behavior under high-speed load combining mechanical experiments and Finite Element Method (FEM). On a microscale, the fracture surfaces are examined by the Scanning Electron Microscopy (SEM).

2. EXPERIMENTAL PROCEDURE

The target material studied in this paper is aluminum alloy Al-Si-Cu and its chemical composition is listed in Table 1.

Table 1. Mass fraction of chemical composition of ADC12 aluminum alloy (wt%)

Si	Cu	Mn	Mg	Fe	Ni	Zn	Pb	Sn	Al
9.6~12.0	1.5~3.5	≤0.5	≤0.3	≤1.2	≤0.5	≤1.0	≤0.1	≤0.1	Bal.

2.1. Quasi-static tensile experiments

To study the mechanical properties of ADC12 aluminum alloy under different stress triaxiality [19], we conducted different types of experiments including tensile and compressive experiments. The tensile experiments include solid bar tensile, notched and shearing experiments.

Tensile specimens were fabricated on a linear cutting machine and the compression specimens were turned into a cylinder with a diameter of 8 mm. The geometries and structures of those specimens are shown in Fig. 1. Experiments were performed in the ETM504C computer-controlled electronic universal testing machine. For tensile experiments, the velocity was 0.21 mm/min and the strain rate was 0.0001/s. The velocity for compression experiments was 1 mm/min.

The stress and strain curves of quasi-static tensile experiments at room temperature are shown in Fig. 2. For solid bar tensile experiment, the ultimate tensile strain is 0.02 (see Fig. 2(a)), which indicates that the ADC12 aluminum alloy is a typical brittle metal. For notched experiments, ultimate tensile strain of 4 mm notch radius specimen is smaller than that of 8 mm notch radius specimen.

The ultimate tensile strain of shear experiment is 10 times smaller than that of solid bar tensile experiment (Fig. 2(a)), illustrating that the specimen tends to fracture under shear stress more than under tensile stress. The ultimate tensile strain in compressive experiment (see Fig. 2(b)) is 10 times greater
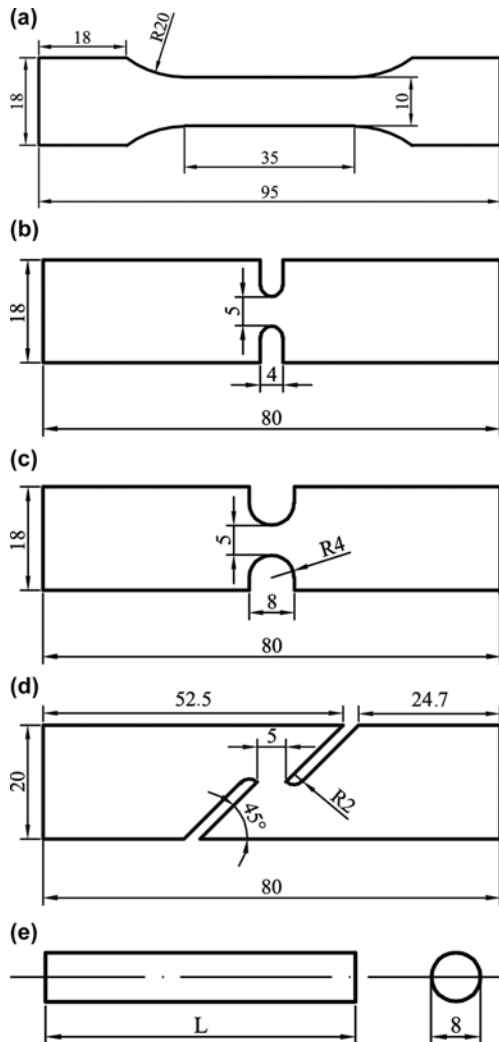

Fig. 1. Sketches of the specimens for quasi-static tensile experiments (unit in mm); (a) Solid bar tensile specimen (thickness = 4 mm) (b) 4 mm notched specimen (thickness = 2.6 mm); (c) 8 mm notched specimen (thickness = 2.6 mm); (d) Shear specimen (thickness = 2.6 mm); and (e) Compression specimen (L = 8, 16, 20 mm).
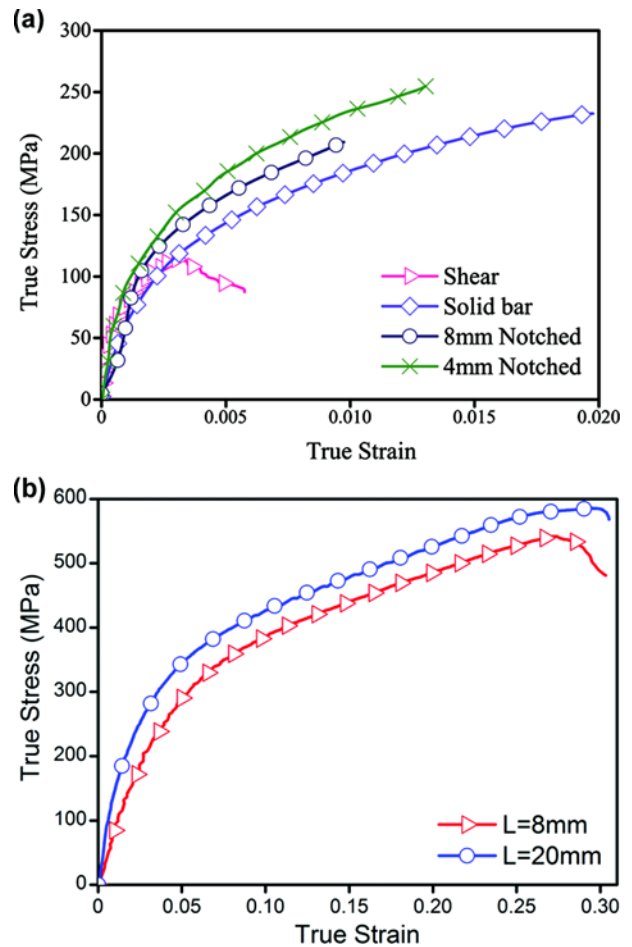

Fig. 2. Stress-strain curves at different stress states: (a) Stress-strain curves for shear, solid bar tensile, 8 mm notched, 4 mm notched experiments and; (b) Stress-strain curves for compression experiments.

Table 2. Experimental data under different stress triaxiality

Experimental Type	Stress Triaxiality (σ^*)	Effective Fracture Plastic Strain (ε_{eff}^f)
Compression	-0.33	0.217
Shear	0.02	0.0025
Solid bar tension	0.33	0.0153
8 mm notched	0.43	0.011
4 mm notched	0.51	0.0072

Fig. 4. Stress-strain curves at different strain rates: (a) Stress–strain curves at low and medium strain rates; and (b) Stress–strain curves at high strain rates.

than that in solid bar tensile experiment (Fig. 2(a)). The lengths of the compression specimens are 8 mm and 20 mm, the compression strength are 539 MPa and 583 MPa, respectively (see Fig. 2(b)). The strength is nearly the same, and it shows that the tensile strength has not been influenced by the dimension of the specimen.

Table 2 list the experimental data of σ^* and ε_{eff}^f. ε_{eff}^f is the effective plastic strain at fracture which is also known as the ultimate tensile strain, calculated from the strain at fracture points in Fig. 2. σ^* is the stress triaxiality, which is calculated from smallest cross-section of quasi-static tensile specimens by LS-Dyna. As shown in the table, with increasing stress triaxiality, the ε_{eff}^f decreases sharply at first and remains stable afterwards.

2.2. Dynamic tensile experiments

The size and geometry of the dynamic tensile experiments were shown in Fig. 3. At room temperature, dynamic tensile experiments were conducted on Zwick HTM 5020 high speed testing machine at different nominal strain rates, namely 0.0005 /s, 0.1 /s, 1 /s, 100 /s, 200 /s, 250 /s, 500 /s and 800 /s.

The brittle metallic specimens tend to rupture before the strain rate reaches the nominal strain rate. The true strain rate, which is the average strain rate from yield point to the fracture
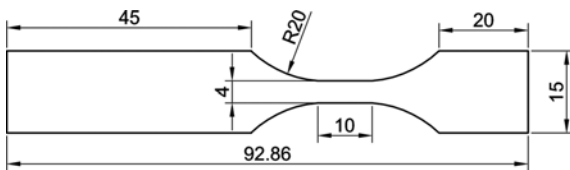

Fig. 3. Sketch of the specimen for dynamic tensile experiments (unit in mm, thickness = 2 mm).

point, is employed in the subsequent FEM analysis and is simplified as strain rate in our literature later. These values are 0.0002 /s, 0.07 /s, 0.35 /s, 60 /s, 180 /s, 220 /s, 400 /s and 650 /s, respectively.

The true stress and true strain curves at different strain rates are shown in Fig. 4. The curves at low and medium rates are shown in Fig. 4(a). According to the figure, the elastic limit reaches 115 MPa and the tensile strength reaches 230 MPa. Besides, the yield strength and tensile strength are almost the same at the rate ranging from 0.0002 /s to 60 /s.

The stress and strain curves at high rates are shown in Fig.

Table 3. Experimental data of tensile experiments at different strain rates

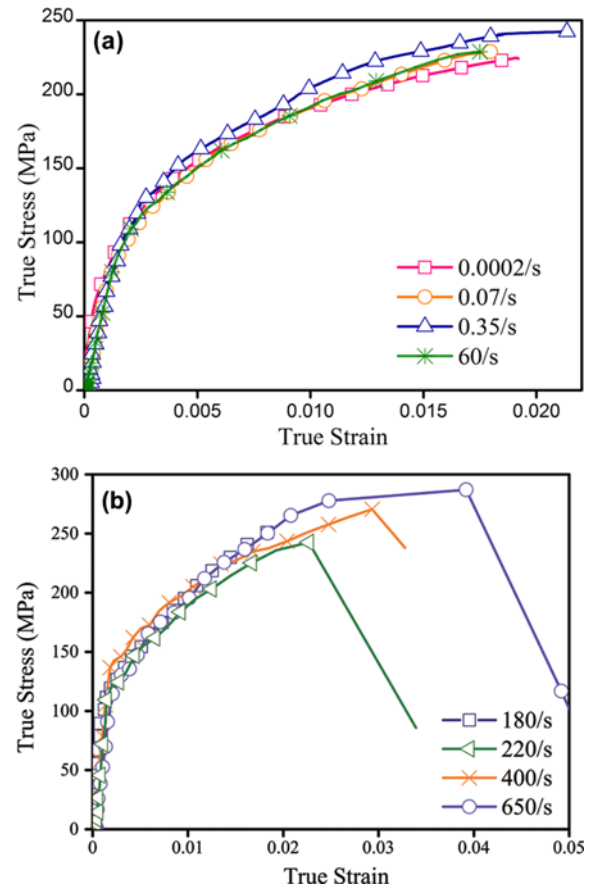| Tensile Velocity (mm/s)	Predicted Strain Rate (/s)	Recorded Strain Rate (/s)	σ_t^f (MPa)	ε_{eff}^f
5E-3	5E-4	2E-4	231	0.0176
1	0.1	0.07	229	0.0161
10	1	0.35	236	0.0143
1000	100	60	232	0.0158
2000	200	180	263	0.0182
2500	250	220	248	0.0207
5000	500	400	285	0.0293
8000	800	650	298	0.0363

4(b). The figure indicates three trends. First, the curves almost coincide with each other at rates 180 /s and 650 /s. Second, curves at 180 /s, 220 /s and 650 /s are almost the same before the true strain reaches 0.01. Finally, ADC12 alloy shows the strain rate sensitivity to true strain.

ε_{eff}^{f} and σ_{t}^{f} at different strain rates are listed in Table 3. ε_{eff}^{f} is the tensile strength, which is the maximum stress that a material can withstand. At low and medium strain rates, ε_{eff}^{f} and σ_{t}^{f} increase slightly with the increasing strain rate. This means ADC12 aluminium alloy is insensitive to strain rate at low and medium rates, coinciding with Refs. [20, 21]. However, when tensile velocity is over 2000 mm/s, σ_{t}^{f} and the ε_{eff}^{f} increase little with the rate increases. The reason of strain rate sensitivity is that the slip processes in crystals are impeded with the strain rate increases. Consequently, we can safely conclude that ADC12 aluminium alloy shows no strain rate sensitivity at low and medium strain rates ($\dot{\varepsilon} \leq 60/s$), but it shows sensitivity at high strain rates ($\dot{\varepsilon} > 60/s$).

3. FRACTOGRAPHY

The fracture surfaces of the tensile specimen were examined, photographed and interpreted under the Carl Zeiss AURIGA Cross Beam Focused Ion Beam Microscope (FIB-SEM) (see Fig. 5). The amplified factors of the SEM photographs ranges from 12 to 10^{7}. From the fracture morphology,
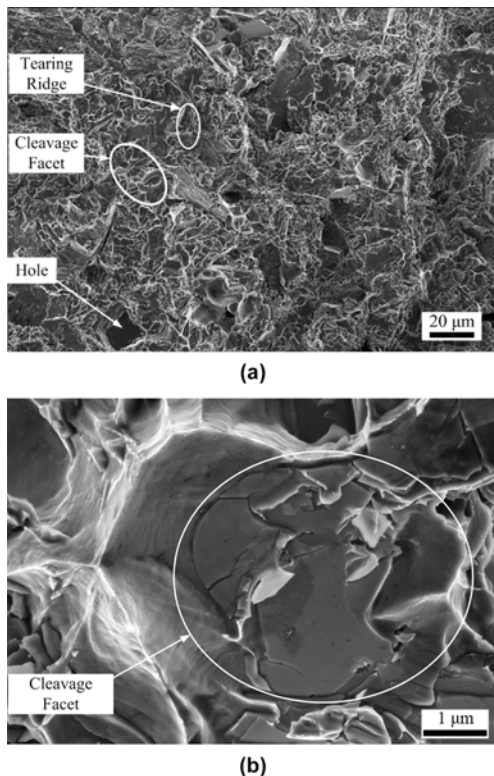

Fig. 5. Fracture morphology for solid bar tensile specimen at different amplified factors: (a) Amplified factors = 500; and (b) Amplified factors = 10000.
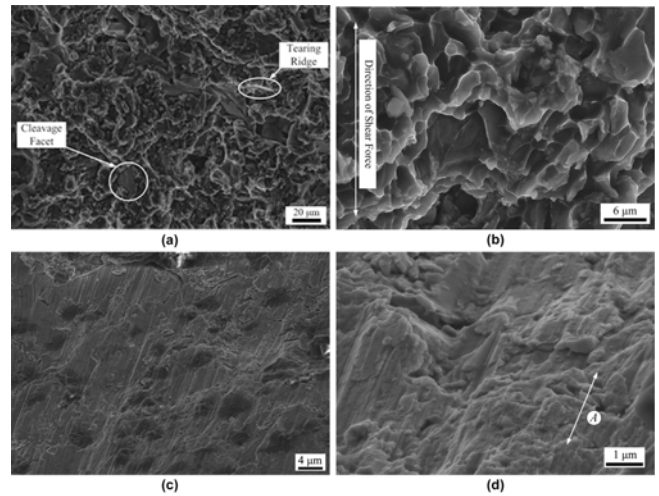

Fig. 6. Fracture morphology for shear and compression specimens: (a) Shear specimen (amplified factors = 500); (b) Shear specimen (amplified factors = 2500); (c) Compression specimen (amplified factors = 2000); and (d) Compression specimen (amplified factors = 10000).

we examine the fracture features of various specimens under different load conditions including tensile, compressive and dynamic tensile experiments. The tensile experiments contain solid bar tensile, notched and shearing experiments.

3.1. Quasi-static tensile experiments

Typical fractographs at 500× and 10000× of solid bar tensile fracture surface are shown in Fig. 5. Overall fracture morphology at lower magnification appears to be rough with features of cleavage facets, tearing ridges and a small number of holes (see Fig. 5(a)). Under tensile loading, this alloy splits along the crystallographic structural plane, namely cleavage facets. These relatively weak facets are the result of regular location of atoms and ions. These facets could be seen by a closer observation of the fracture surface (see Fig. 5(b)). Combining cleavage facets and tearing ridges, we safely conclude that fracture is a typical quasi-cleavage fracture, which indicates the rupture of ADC12 alloy is brittle.

The fracture morphologies of shear and compressive specimens are shown in Fig. 6. A large number of cleavage facets and tearing ridges can be observed (see Figs. 6(a,b)). The direction of tearing ridges is nearly parallel to the direction of shear force, indicating the shear force is the driving force. The fracture morphologies of the compression specimen are shown in Figs. 6(c,d). From these figures we could distinguish shear plane. Figure 6(d) is a closer observation of shear plane and the arrow A represents the direction of shear force, which is coincided with the direction of shear plane. This phenomenon indicates that the driving force of the fractured process in compression experiment is the shear force too.

3.2. Dynamic tensile experiments

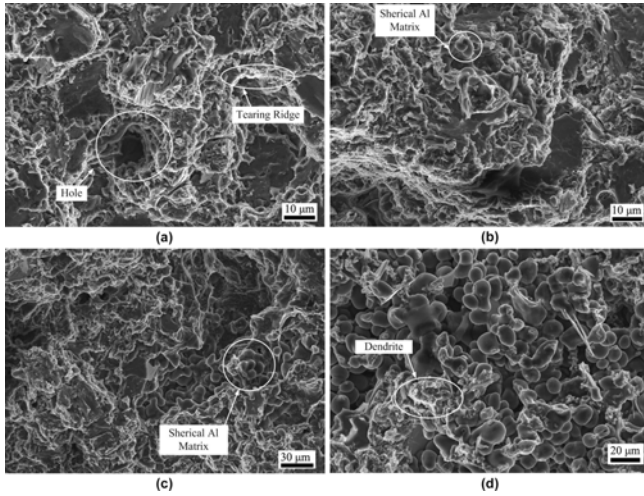Fractographs of the fracture surfaces at low and medium

Fig. 7. Fracture morphology at different strain rates (amplified factors = 500): (a) 0.07 /s; (b) 60 /s; (c) 220 /s; and (d) 650 /s strain rate.

strain rates with magnification of 500 times are shown in Figs. 7(a, b). These fractographs show a large number of tearing ridges, a small number of holes and inclusions. Besides, a small number of spherical Al matrices are observed in Fig. 7(b). These fracture features indicate the typical quasi-cleavage fracture.

Fractographs at high strain rates are shown in Figs. 7(c,d). Comparing these photographs with the fractographs at low and medial strain rates, not only the tearing ridges could be observed, but an increasing number of spherical Al matrices and dendrites. Under high-speed loading, Al matrices tend to change in grain phase making the slip system in orientation easy to slip, contributing to the slip process and improving the mechanical strength (see Fig. 4(b)).

4. IDENTIFICATION OF THE JOHNSON-COOK PARAMETERS

4.1. Identification of material model parameters

Johnson and Cook [2] proposed an empirical model to study the relationship between the flow stress and influence factors including effective plastic strain, strain rate and temperature. The J-C material model is expressed as

$$\sigma_e = (A + B\bar{\varepsilon}_P^n)\left(1 + C\ln\left(\frac{\dot{\bar{\varepsilon}}_p}{\dot{\varepsilon}_0}\right)\right)(1 - T^{*m}) \tag{1}$$

where σ_e is the Mises flow stress, $\bar{\varepsilon}_p$ is the effective plastic

strain, $\dot{\bar{\varepsilon}}_p$ is the effective plastic strain rate, $\dot{\varepsilon}_0$ is the reference strain rate, A and B are the empirical constants, n is the strain harden constant, C is the strain rate sensitive constant and m is the temperature soften constant. $T^* = (T - T_{room}) / (T_{melt} - T_{room})$, where T_{melt} is the melting point of material and T_{room} is the room temperature.

Because ADC12 aluminum alloy shows weak strain rate sensitivity in stress, it is reasonable to assume $\dot{\bar{\varepsilon}}_p = \dot{\varepsilon}_0$. All the experiment in this paper were performed under room temperature, then Eq. (1) is simplified to

$$\sigma_e = (A + B\bar{\varepsilon}_p^n) \tag{2}$$

For the above three-parameter exponential functional form, a suitable fitting option is based on the least square method. The parameters in the J-C material model are shown in Table 4.

4.2. Identification of failure model parameters

Based on continuum mechanics, the J-C failure criterion was first proposed by Johnson and Cook [14]. Based on the criterion, the fracture model in commercial software LS-Dyna is modified by adding a constant named EFMIN, which is the lower-bound for strain at fracture [22]. Then, the model is expressed as

$$\varepsilon_{eff}^f = \max([D_1 + D_2e^{D_3\sigma^*}][1 + D_4\ln\dot{\varepsilon}^*], EFMIN) \tag{3}$$

where D_1, D_2, D_3, D_4 and D_5 are empirical constants and $\sigma^* = P / \sigma_{eff}$ is the stress triaxiality with P being the hydrostatic pressure and σ_{eff} being the effective plastic stress.

The empirical parameters D_1, D_2, D_3, D_4, $\dot{\varepsilon}_0$ and EFMIN can be obtained by experimental data in Tables 2 and 3. $\dot{\varepsilon}_0$ equals 98 /s which is the threshold strain rate between medium and high strain rates (see Fig. 4), and has a noticeable influence on flow stress [23]. Above all, the fitted parameters of the J-C material model and failure model are shown in Table 4.

5. FEM SIMULATIONS AND EXPERIMENTAL VALIDATIONS

To validate parameters in the J-C model, simulations incorporating the J-C model and obtained parameters were conducted. We compared the simulation and experimental results in two aspects, namely the fractured position and the strain-stress curve.

Table 4. ADC12 material parameters for Johnson-Cook model

Johnson-Cook	Constants of Models					
Material model	A/ MPa	B/ MPa	n	C	m	$\dot{\varepsilon}_0$
	115.7	1644.6	0.6232	0	0	98
Fracture model	D_1	D_2	D_3	D_4	D_5	EFMIN
	0.00939	0.00001	-29.4	1.5	0	0.01537

5.1. Quasi-static tensile FEM simulation

The quasi-static tensile specimens were meshed with hexahedral solid elements. In more details, the average element length in solid bar tensile specimens was 0.3 mm, and the length of notched and shear specimens was 0.5 mm. Empirical constants for ADC12 material are provided in Table 4. In addition, the elastic modulus, density and poisson's ratio for ADC12 material are 71 GPa, 2.7070×10^3 kg/m^3, and 0.36 respectively. The bulk behavior of the material is determined by GRUNEISEN and corresponding parameters for ADC12 material are given in Ref. [24]. Comparisons between the experimental data and simulation results of fractured specimens are shown in Fig.
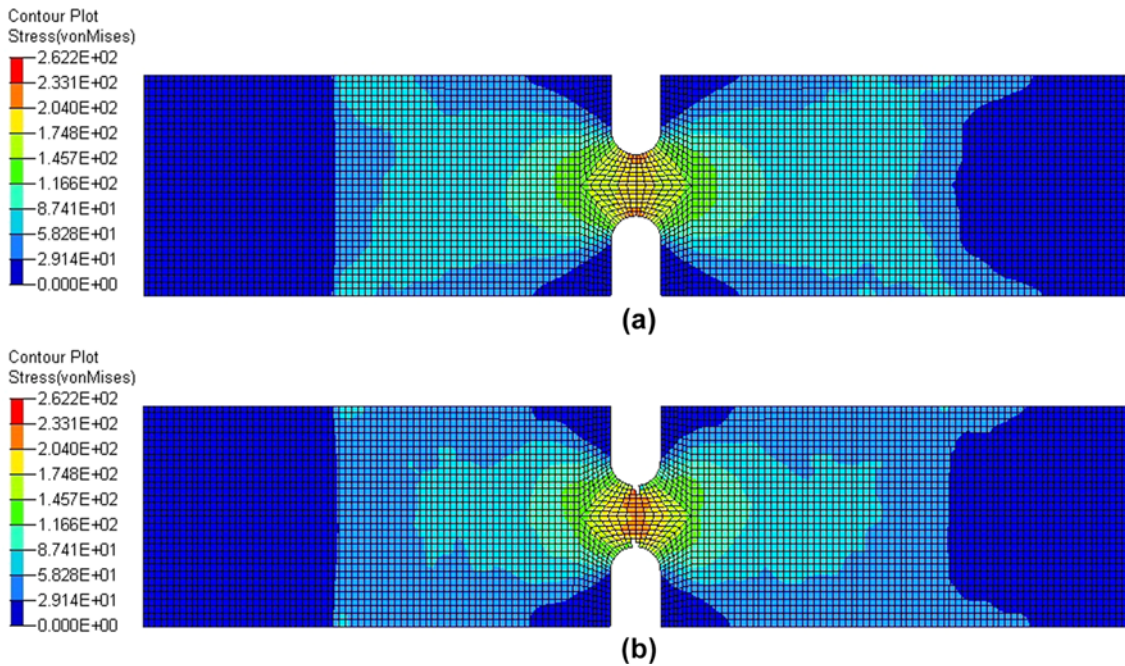
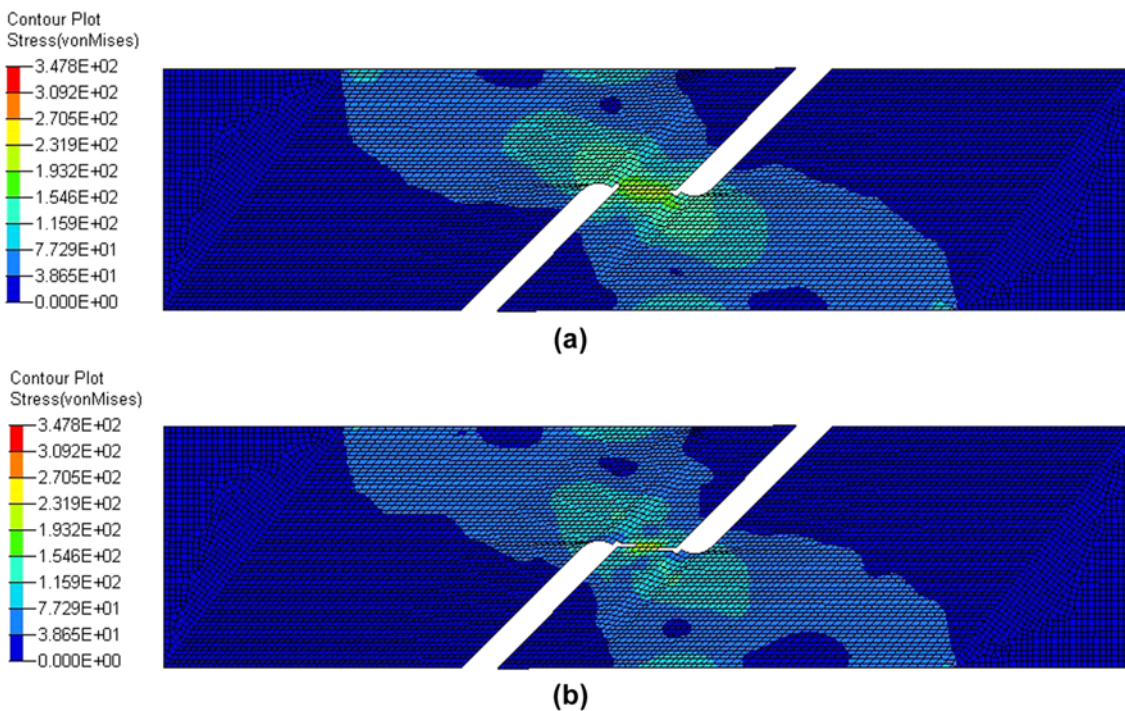**Fig. 8.** Von-Mises stress contour plots of 4 mm notched specimen at (a) $t = 0.015335$ s; (b) $t = 0.015337$ s.

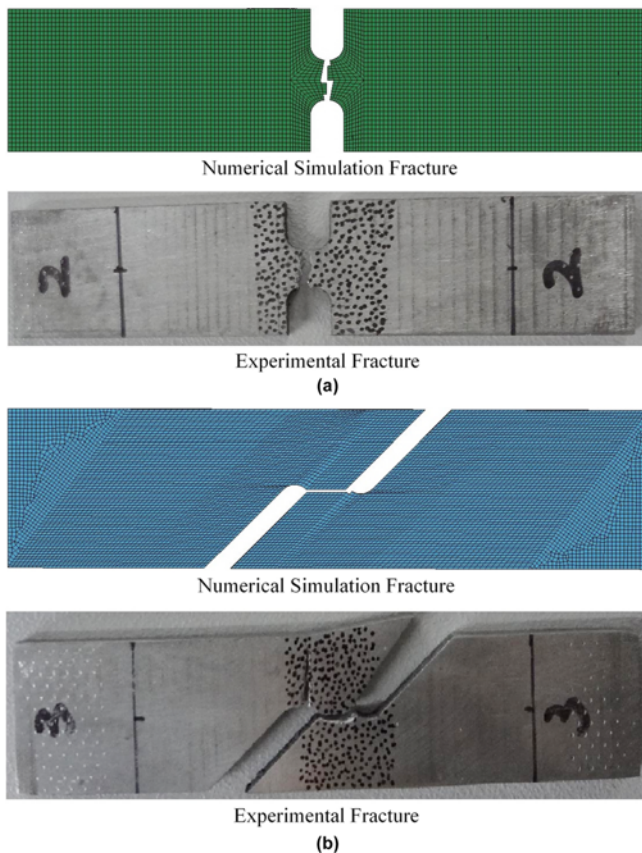**Fig. 9.** Von Mises Stress contour plots of shear specimen at (a) $t = 0.01573$ s; and (b) $t = 0.01574$ s.

Fig. 10. Comparisons between the simulations and experiments of fractured specimens: (a) 4 mm notched experiment; and (b) Shear experiment.

Fig. 11. Comparisons between simulations and experiments of stress-strain curves: (a) 4 mm notched experiment; and (b) shear experiment.

10 and the stress and strain curves are shown in Fig. 11.

In the 4 mm notched experiment, the von Mises stress contour plots at different times are shown in Fig. 8. It can be observed from the figure that the stress mainly distributes in the minimum cross section before rupture. The crack initiates from the edges of the minimum cross section, and develops along stress intense area. The ruptured position is in the minimum cross section and there is no necking phenomenon (see Fig. 10(a)). Obviously, the fracture pattern in simulation matches the experimental one which is shown in Fig. 10(a). Moreover, the stress-strain curve in simulation is in accordance with that in experiment (see Fig. 11(a)).

The von Mises stress contour plot of shear experiment at different times is shown in Fig. 9. The comparisons between simulation and experiment of the fractured specimens is shown in Fig. 10(b). The fractured position in simulation is in the minimum cross section which is the stress intense area before rupture. This phenomenon is similar to experimental results, but there is another fractured surface which is perpendicular to the one in the minimum cross-section. The surface cannot be observed in simulation. Reasons may lie behind the stress concentr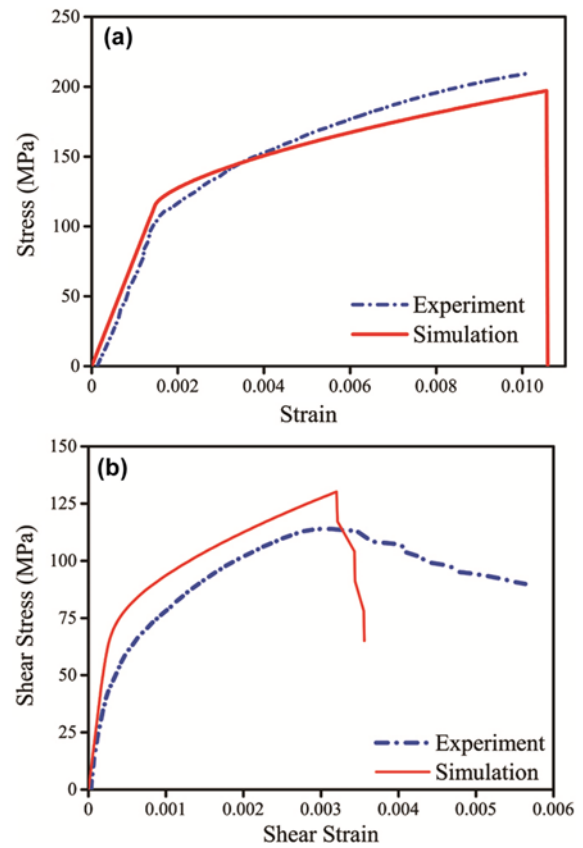ation at transition section. The stress distribution in the surrounding area of the transition section is altered. Due to the stress concentration, the cracks initiated from the fillets and propagated under shear load. Finally, transverse and longitudinal failures occurred. This experimental phenomenon indicates that there are two kinds of fracture modes, which is shear and tensile fracture respectively. Contrarily, since there is no stress concentration in the fillet area in simulation and one fracture mode exists in the J-C fracture model, the transverse and longitudinal fractures cannot occur simultaneously. Therefore, there is only one crack in the minimum cross section in simulation. Perhaps for the same reason, in Fig. 11(b), larger stress occurs in simulation than that in the experiment. Apart from this, the overall trend between simulation and experiment is nearly the same.

5.2. Dynamic tensile FEM simulation

Because the fractured specimens at different strain rates are similar to each other, we only compare the FEM simulation and experimental results at 0.35 /s and 220 /s. From Fig. 12, gauged length shows stress intensity during deforming process. Fractured positions are all in gauged length with no clear necking phenomenon (see Fig. 13(a)). From Fig. 13, it is easily to conclude that the simulation results show good agreement with experimental results.
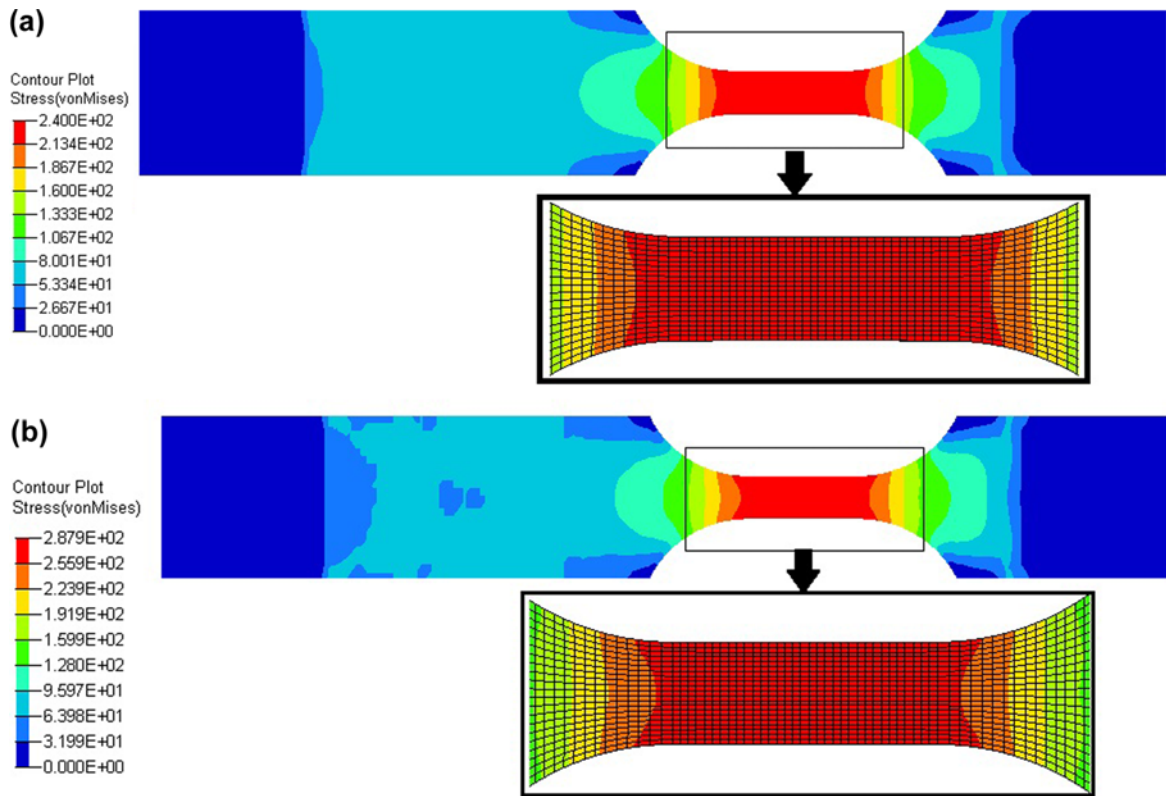
Fig. 12. Von Mises stress contour plots of dynamic tensile specimen (a) under 0.35 /s at 0.38 ms; and (b) under 220 /s at 0.118 ms.
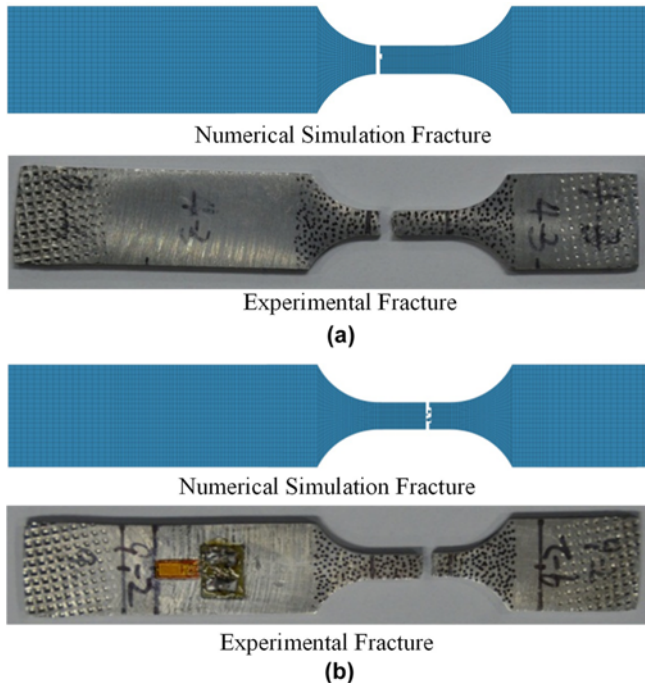

Fig. 13. Comparisons between the simulations and experiments of fractured specimens at: (a) 0.35 /s strain rate; and (b) 220 /s strain rate.

The stress and strain curves at different strain rates are shown in Fig. 14. ADC12 material showed weak strain rate sensitivity at low and medium rates. Consequently, one simulation curve, on behalf of curves at these rates, is compared with experimental curves from 0.0002 /s to 60 /s (see Fig. 14(a)). The curve in simulation agrees with the experimental curves in elastic region, strain hardening region and fracture point. The stress and strain curves at high strain rates in simulation are coincided with the experimental data (see Figs. 14(b-e)).

6. APPLICATION

The J-C model and following parameters are found to appreciably represent the FEM simulation of an engine mount bracket (EMB) crashing process. The function of EMB is to connect the engine with a frame. Fig. 18 shows an EMB fixed to an engine, and the EMB is made of ADC12 material. In a frontal crash, EMB was aiming for an instantaneous fracture in a predicted sequence, making the engine fall apart. Subsequently, adequate space was spared for front rail to deform and absorb crashing energy, protecting occupants from accidents.

The EMB is installed on vehicle frame by three bolts. In a frontal crash, the engine is subjected to backward impact load and the EMB is suffered from shear load in turn (see Fig. 15(a)), where F_s represents shear load. Simulation of the full scale vehicle crash is not suitable to predict the fracture behavior of EMB, and some simplifications should be taken.
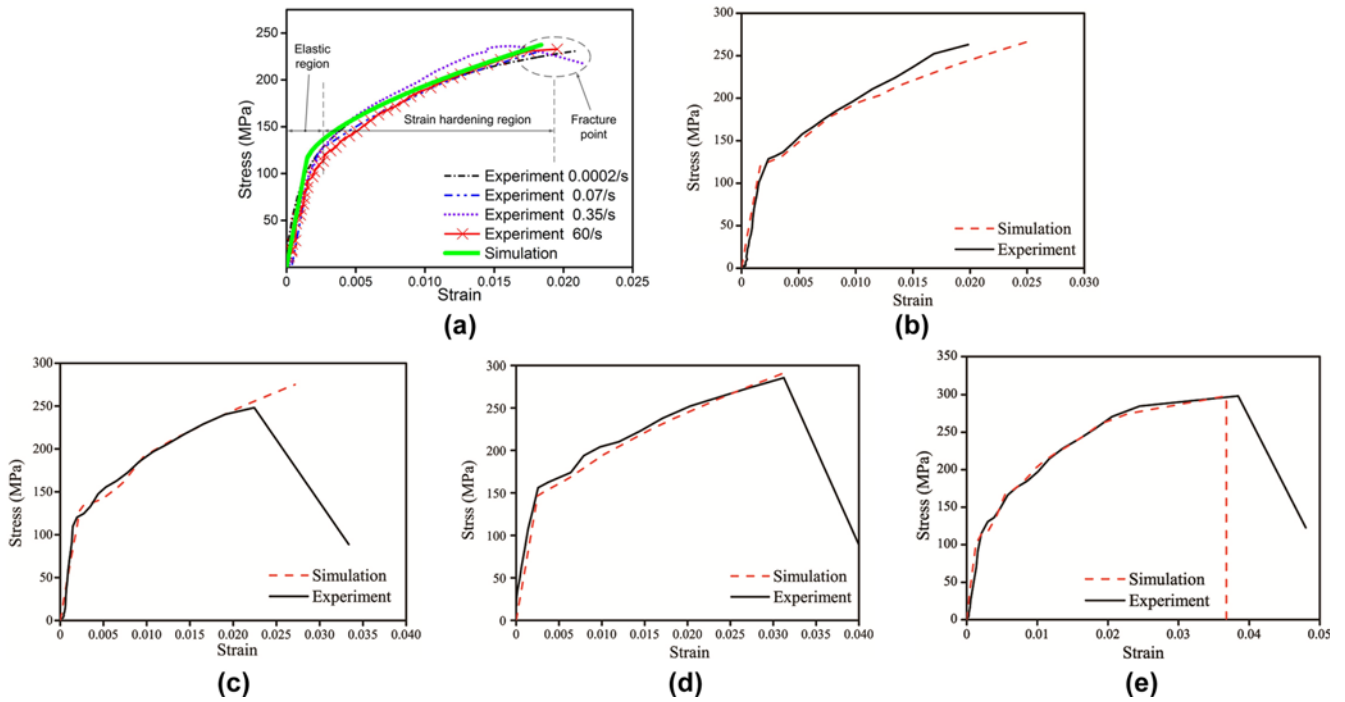
Fig. 14. Comparisons between experiments and simulations of stress-strain curves at: (a) Low and medium strain rates; (b) 180/s strain rate; (c) 220 /s strain rate; (d) 400/s strain rate; and (e) 650/s strain rate.
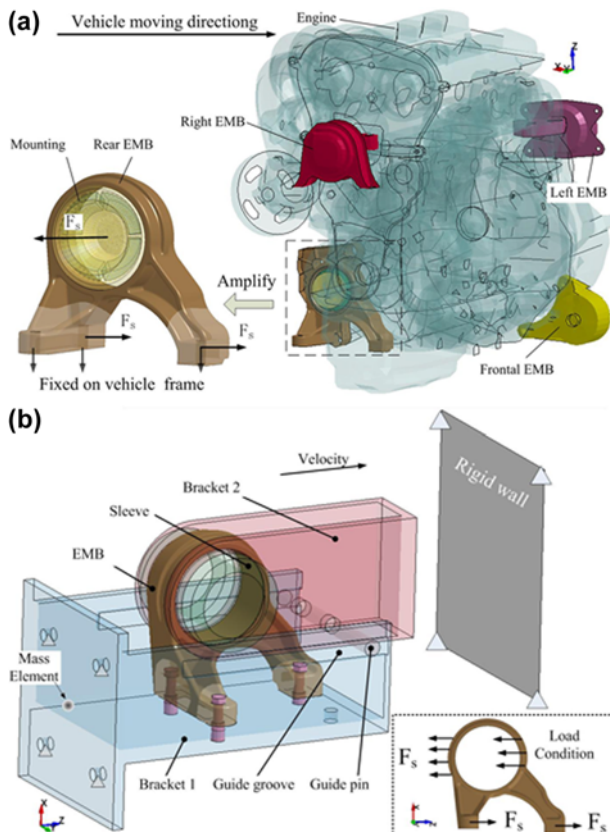

Fig. 15. EMB under impacting load: (a) Relative position of EMB mounted in vehicle frame; and (b) FEM model of the assembly fixture and a magnified observation of the EMB.

Figure 15(b) is an assembly fixture to simulate the EMB under impact loading in the frontal crash. The fixture is made up of four parts that is the drawer-like bracket 1, bracket 2, a guide pin and a sleeve (see Fig. 15(b)). The Finite Element (FE) model of the fixture consisted of 23223 pentahedral elements and 1522 hexahedral elements. The average element length in contact section was 0.5 mm. The failure of the EMB was simulated by deleting elements, and the average length was 1 mm contributing to the high accuracy in crashing simulation. The mass of sled carriage (see Fig. 15(b)) was added to the bracket 1 by mass elements. The nodes on the bracket 1 were constrained except Z direction with velocity given as 10 m/s. The J-C model was used to describe the deformation of EMB and the J-C failure model was used as the criterion for the deletions of elements with the parameters in Table 4. The von Mises stress contour plots of EMB at different times is shown in Fig. 16. From those figures, the deforming process and fracture surfaces can be easily distinguished. Max-stress arises from section A firstly. Subsequently, crack initiates from inner area and the propagate along section A till failure. After section A fractured, section B is the stress intense area till rupture. After sections A and B are fractured, section C is the stress intense area following the fracture at 0.00941s.

Crashing experiments are conducted to validate simulation results. Fixtures, sled carriage and other experimental equipment are shown in Fig. 17. The EMB is fixed in bracket 1 which mounts on the sled carriage. During the crashing experiment, the sled crashed into rigid wall at a velocity of 10 km/h. The
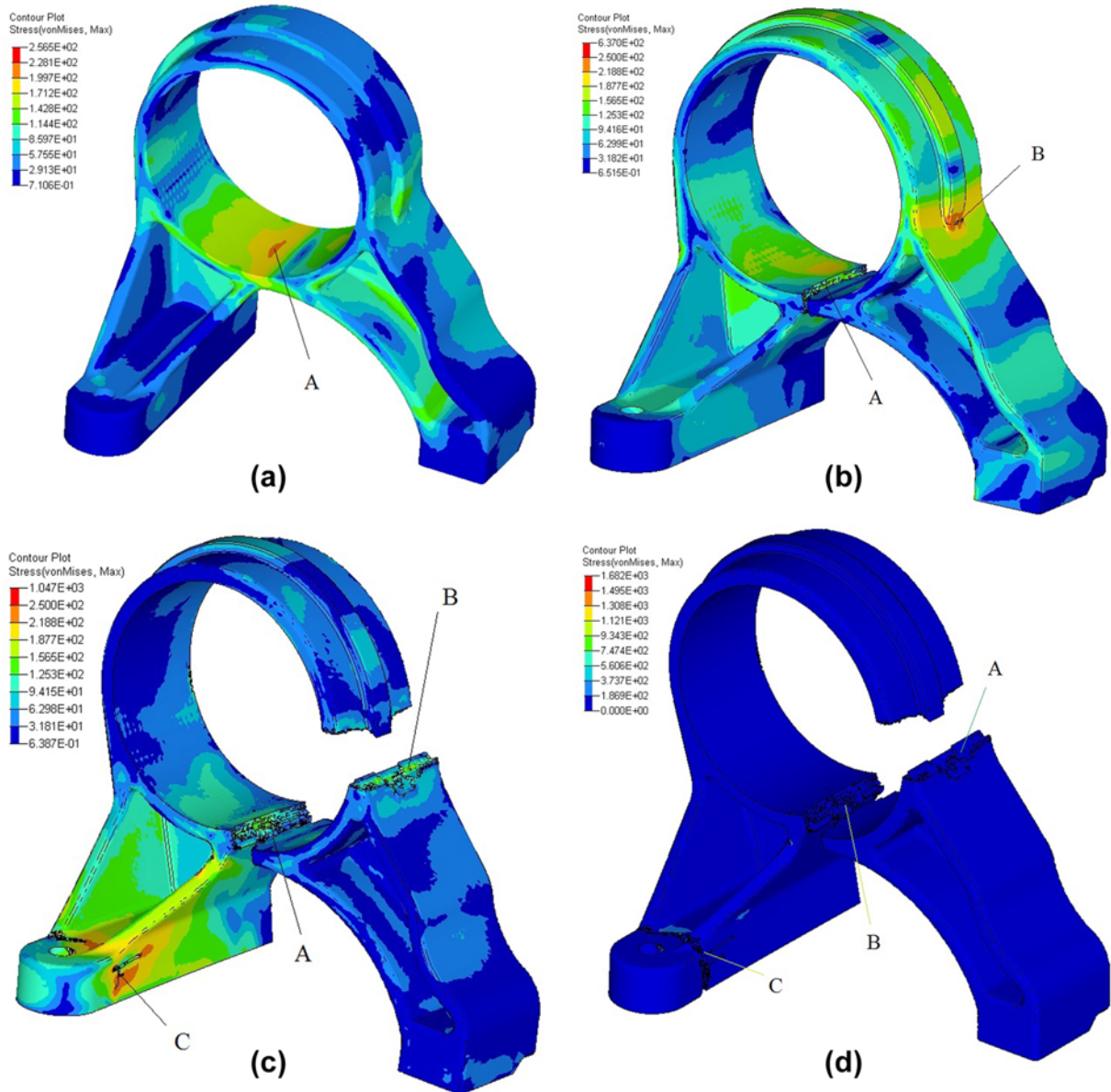
Fig. 16. Von Mises Stress distribution of EMB under impact loading at: (a) *t* = 0.0034 s; (b) *t* = 0.00427 s; (c) *t* = 0.00918 s; and (d) *t* = 0.00941 s.
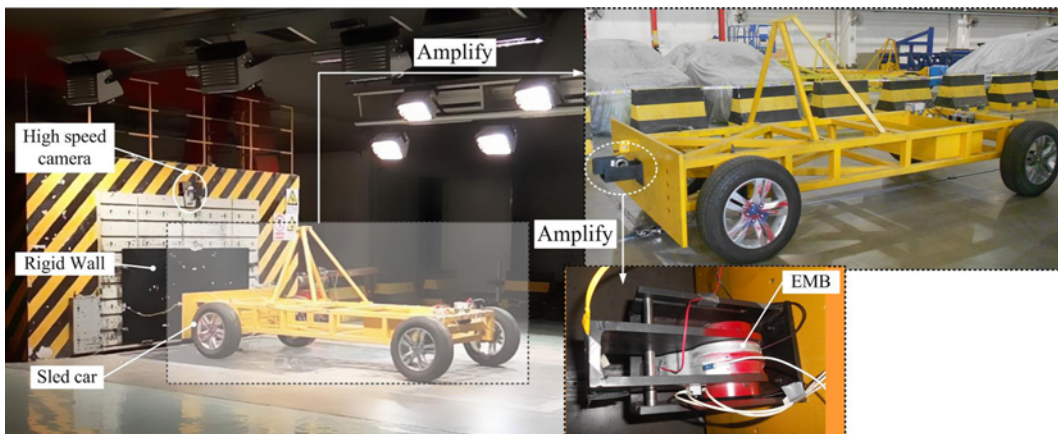

Fig. 17. Detail of crashing experiment setups with magnified view of fixture assembly and EMB.
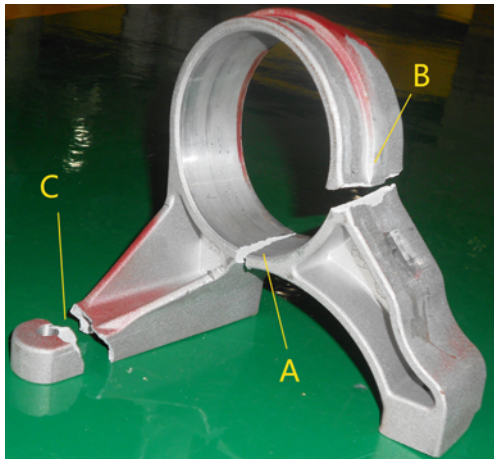
Fig. 18. Fractured EMB after impacting experiment.

whole impacting process was recorded by high speed cameras. When the bracket 2 impacted on the rigid wall, the EMB was under shear load induced by the sleeve.

The fractured EMB of experiment is shown in Fig. 18. It breaks into three sections, which is sections A, B and C respectively. The simulation results (Fig. 16(d)) are in good agreements with experiment results (Fig. 18). The accordance of crashing results in simulation and experiment indicates that the J-C model and parameters can successfully predict the damage and fracture process of ADC12 brittle metal under impact load.

7. CONCLUSIONS

A series of tensile and compressive experiments are performed to extract parameters of the Johnson-Cook model, which are employed in the subsequent FEM studies. Mechanical behaviors are studied by those experiments. The tensile experimental data shows that the flow stress of ADC12 material is pertinent to strain rate and stress triaxiality. Additionally, the fracture morphology of the SEM images reveals the quasi-cleavage fracture indicating the brittleness of ADC12 alloy. FEM simulation of these tensile and compression experiments are also conducted. The simulation results agree with the experimental data. The results from the crash simulation, substantiated by tensile and compression tests presented herein, are in good agreement with the experimental crash test. Consequently, this work provides a feasible approach in simulating the deformation and fracture process of brittle metals.

ACKNOWLEDGMENT

REFERENCES

1. J. K. Gran, A. L. Florence, and J. D. Colton, *J. Eng. Mech.* **115**, 891 (1989).
2. Z. Han and G. Gerard, *Int. J. Solids. Struct.* **33**, 3363 (1996).
3. A. Domenico, C. Ezio and P. Andrea, *Int. J. Rock. Mech. Min.* **46**, 514 (2009).
4. G. R. Johnson and T. J. Holmquist, *High Pressure Science and Technology.* **309**, 981 (1994).
5. H. Jiang and M. G. Chorzepa, *Eng. Fail. Anal.* **55**, 63 (2015).
6. A. Banerjee, S. Dhar, S. Acharyya, D. Datta, and N. Nayak, *Mater. Sci. Eng. A* **640**, 200 (2015).
7. A. E. Buzyurkin, I. L. Gladky, and E. I. Kraus, *Aerosp. Sci. Technol.* **45**, 121 (2015).
8. J. Tan, M. Zhan, S. Liu, T. Huang, J. Guo, and H. Yang, *Mater. Sci. Eng. A* **631**, 214 (2015).
9. D. Zhang, Q. Shangguan, C. Xie, and F. Liu, *J. Alloys Compd.* **619**, 186 (2015).
10. Tomasz Wierzbicki, Yingbin Bao, Young-Woong Lee, and Y. Bai, *Int. J. Mech. Sci.* **47**, 719 (2005).
11. F. J. Zerilli and R. W. Armstrong, *J. Appl. Phys.* **61**, 1816 (1987).
12. J. Choung, W. Nam, and J. Y. Lee, *Mar. Struct.* **32**, 49 (2013).
13. G. R. Johnson and W. H. Cook, *Eng. Fract. Mech.* **21**, 31 (1985).
14. J. Xiao and D. Shu, *Met. Mater. Int.* **21**, 823 (2015).
15. B. Yingbin and T. Wierzbicki, *J. Eng. Mater. Technol.* **126**, 314 (2004).
16. G. C. Sih and H. Liebowitz, *Int. J. Solids. Struct.* **3**, 1 (1967).
17. G. C. Sih and B. Macdonald, *Eng. Fract. Mech.* **6**, 361 (1974).
18. S. Raymond, *Eng. Anal. Bound. Elem.* **42**, 20 (2014).
19. X. Jin, S. Chaiyat, L. M. Keer, and K. Kiattikomol, *J. Mech. Phys. Solids.* **56**, 1127 (2008).
20. S. Nemat-Nasser, *ASM Handbook Volume 8: Mechanical Testing and Evaluation, Introduction to High Strain Rate Testing*, pp. 427-428, ASM International, Ohio, USA (2000).
21. T. Mukai, K. Ishikawa, and K. Higashi, *Mater. Sci. Eng. A* **204**, 12 (1995).
22. LSTC, *LS-DYNA keyword user's manual Volume 2 Material models*, pp.2.113-112.115, Livermore Software Technology Corporation, California, USA (2014).
23. L. Schwer, *Optional Strain-Rate Forms for the Johnson Cook Constitutive Model and the Role of the Parameter Epsilon_01*, p.1.110, Livermore Software Technology Corporation, Frankenthal, Germany (2007)
24. D. J. Steinberg, *Equation of State and Strength Properties of Selected Materials*, pp.4.0-5.9, Lawrence Livermore National Laboratory, California, USA (1991).